Majorana Entanglement Bridge

Stephan Plugge,[1] Alex Zazunov,[1] Pasquale Sodano,[2,3,4] and Reinhold Egger[1,2]

[1]*Institut für Theoretische Physik, Heinrich-Heine-Universität, D-40225 Düsseldorf, Germany*
[2]*International Institute of Physics, Universidade Federal do Rio Grande do Norte, 59078-400 Natal-RN, Brazil*
[3]*Departamento de Fisica Téorica e Experimental,*
Universidade Federal do Rio Grande do Norte, 59072-970 Natal-RN, Brazil
[4]*INFN, Sezione di Perugia, Via A. Pascoli, 06123 Perugia, Italy*
(Dated: June 2, 2015)

We study the concurrence of entanglement between two quantum dots in contact to Majorana bound states on a floating superconducting island. The distance between the Majorana states, the charging energy of the island, and the average island charge are shown to be decisive parameters for the efficiency of entanglement generation. We find that long-range entanglement with basically distance-independent concurrence is possible over wide parameter regions, where the proposed setup realizes a "Majorana entanglement bridge". We also study the time-dependent concurrence obtained after one of the tunnel couplings is suddenly switched on, which reveals the timescales for generating entanglement. Accurate analytical expressions for the concurrence are derived both for the static and the time-dependent case. Our results indicate that entanglement formation in interacting Majorana devices can be fully understood in terms of an interplay of elastic cotunneling (also referred to as "teleportation") and crossed Andreev reflection processes.

I. INTRODUCTION

Over the past few years, the prospect of realizing Majorana bound states (MBSs) in superconducting hybrid devices has attracted a lot of attention, see Refs. [1–3] for reviews. MBSs are predicted to emerge, for instance, as end states in proximitized one-dimensional Rashba nanowires in a magnetic Zeeman field, where signatures for their existence have already been reported in transport experiments [4–10]. For these topologically superconducting (TS) nanowires, MBSs are located at the respective ends of the wire, and the overlap between their wavefunctions becomes exponentially small for large nanowire length L. MBSs can then intuitively be thought of as spatially separated "half fermions". They are under discussion as basic ingredients for "topological" qubits in quantum information applications, where information is nonlocally stored and, thus, should be quite robust against local decoherence processes. Systems with MBSs are also predicted to allow for non-Abelian Ising anyon braiding statistics. Since Ising anyons do not allow for universal quantum computation by themselves, it is essential to thoroughly understand the physics of Majorana states coupled to conventional qubits, where the latter can be realized in terms of nanoscale quantum dots [11–18].

Majorana bound states are described by self-adjoint operators, $\gamma_j = \gamma_j^\dagger$, which anticommute with each other, $\{\gamma_j, \gamma_k\} = \delta_{jk}$, and with all other fermion operators. A pair of MBSs effectively forms a single nonlocal fermion with annihilation operator

$$f = (\gamma_1 + i\gamma_2)/\sqrt{2}, \qquad (1)$$

where the eigenvalue $n_f = 0, 1$ of the number operator

$$\hat{n}_f = f^\dagger f = i\gamma_1\gamma_2 + 1/2 \qquad (2)$$

describes the state of the MBS pair [1]. For large L, the hybridization energy between the MBSs forming this pair becomes exponentially small,

$$\epsilon_f \sim \exp(-L/\xi). \qquad (3)$$

The length ξ refers to the spatial size of a MBS and is related to the superconducting coherence length in the proximitized nanowire [1]. For $L \to \infty$, the MBS pair is then equivalent to a single zero-energy fermion.

In this work, we consider the simplest case of a single MBS pair and study the concurrence of entanglement, C, between two single-level quantum dots [19] tunnel-coupled to the MBSs, see Fig. 1 for a schematic illustration of the setup. Entanglement is a key concept in quantum mechanics and represents an essential resource for many quantum computation schemes [20]. Two spatially separated systems are said to be entangled when their quantum states cannot be described independently. One may naively expect that because each MBS amounts to half of the same fermion state, the MBSs themselves are strongly entangled. However, this is a meaningless statement since only the MBS pair has a well-defined state representation, see Eq. (1). On the other hand, the nonlocality of the f fermion level suggests that the two dots coupled to the MBSs could be fully entangled. For a grounded superconducting island, where the charging energy E_C is negligible, this question has been studied in Refs. [21–25], and one finds that precisely the opposite statement holds true in the long-distance limit $\epsilon_f \to 0$, i.e., both dots are perfectly disentangled. This result is consistent with the absence of correlations among currents flowing through normal-conducting leads in contact to different MBSs [1, 26].

In what follows, we are especially interested in the possibility of long-range entanglement generation, such that
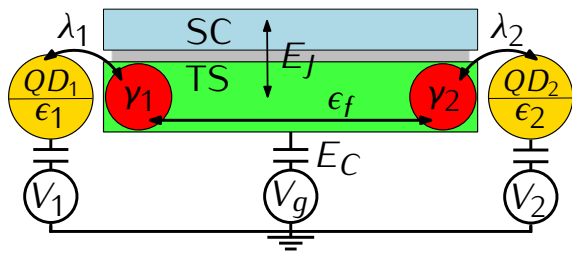
Figure 1. Schematic illustration of the setup. Large circles correspond to two quantum dots (QD$_1$ and QD$_2$), where gate voltages $V_{1,2}$ allow one to vary the energy levels $\epsilon_{1,2}$. A Rashba nanowire is deposited on a superconducting island with charging energy E_C, where the proximity effect in combination with a Zeeman field induces a TS phase. The dimensionless gate parameter n_g (see main text) is proportional to a gate voltage V_g regulating the average charge on the TS island. Small (red) circles represent MBS operators γ_1 and γ_2, where the corresponding wavefunctions are located near the ends of the nanowire and the hybridization ϵ_f corresponds to the distance L between both MBSs, see Eq. (3). Tunnel couplings λ_1 and λ_2 connect the dots to the respective MBSs. In addition, the Josephson energy E_J describes the coupling to another grounded bulk superconductor (SC).

the concurrence $C(L)$ does not decay up to very long dot distance L [21]. We shall determine the detailed conditions for the realization of such a "Majorana entanglement bridge" in the setup shown in Fig. 1. In particular, we find that the charging energy E_C plays an important role in allowing for long-range entanglement generation, i.e., one should work with a mesoscopic floating (not grounded) superconducting island. We note in passing that standard notions of long-range entanglement refer to an exponential decay, $C(L) \sim \exp(-L/\ell)$, and merely require that the lengthscale ℓ is long [27, 28]. In particular, for the topologically trivial limit of our setup, i.e., when the superconducting island does not host MBSs, such an exponential decay of $C(L)$ is expected, see also Ref. [29], where ℓ is equivalent to the superconducting coherence length. The length-independence of $C(L)$ predicted for the device in Fig. 1 holds as long as the charging energy, which scales approximately as $E_C \sim 1/L$ in the TS nanowire geometry, remains the dominant energy scale. In particular, E_C should exceed both the thermal energy $k_B T$ and the MBS hybridization scale ϵ_f in Eq. (3).

Indeed, charging effects can change the physics in a profound way by coupling MBSs to the dynamics of the Cooper pair condensate on the island. In Ref. [30], Fu studied the transmission through a setup as in Fig. 1 but with normal-conducting leads replacing the dots. For large E_C and when the gate voltage is tuned to a Coulomb blockade conductance peak, i.e., the dimensionless parameter n_g regulating the average island charge is half-integer, only two degenerate island charge states are accessible and the model effectively maps to a spinless resonant tunneling problem. In a slight abuse of terminology, the resulting nonlocal phase-coherent transfer of

electrons from one lead to the other has been dubbed "teleportation" (TP) by Fu [30], see also Refs. [31, 32]. However, it has been argued that entanglement may be achieved more efficiently under Coulomb blockade valley conditions, i.e., when n_g stays close to an integer [33–35]. As we discuss in detail below, entanglement is then a consequence of elastic cotunneling [19] processes. In our setup, elastic cotunneling has a strongly nonlocal character due to the underlying MBS realization of the f fermion, and therefore this process has also been referred to as "teleportation" [33, 34], see Sec. III A below. When more than two MBSs are present on the superconducting island, a nonperturbative version of the TP mechanism triggers the so-called topological Kondo effect [36–40]. However, in the present work we shall focus on just one MBS pair, where topological Kondo physics is absent.

Besides TP processes, however, it is well-known that entanglement can also be generated through crossed Andreev reflection (CAR) processes. So far, CAR-induced entanglement in a system as shown in Fig. 1 has only been discussed for the grounded device, where $E_C = 0$. As mentioned above, when also $\epsilon_f = 0$, the dots will be perfectly disentangled, but for finite ϵ_f (and hence not too large L), CAR processes generate entanglement both for the case of normal-conducting leads [21–23, 26] and for the dot case at hand [24, 25]. This entanglement can be probed through the violation of Bell inequalities when several MBS pairs are present [41]. In general terms, CAR refers to the splitting of a Cooper pair on the island which produces entangled electrons on different dots (or leads) [42, 43]. Similarly, in the reverse process, a Cooper pair is created by the combined in-tunneling of electrons from different sides. For normal-conducting leads, local Andreev reflection competes with CAR, since both electrons can be created (or annihilated) also in the same lead, and hence perfect entanglement is not possible [23]. For the single-level dots studied here, however, local Andreev reflection is absent and perfect entanglement due to CAR processes may be realized. Below we address the fate of CAR-generated entanglement as well as the interplay of CAR and TP processes when interactions ($E_C \neq 0$) are important.

In addition, we have also studied the time-dependent concurrence, $C(t)$, found after one tunnel coupling is suddenly switched on. Such a "quench" can be experimentally implemented by changing the voltage on a finger gate in close proximity to the respective tunnel contact, cf. Ref. [4]. By monitoring the time-dependent concurrence, one can achieve a better understanding of the timescales on which entanglement is built up in such a setting [44]. For the setup in Fig. 1 with $E_C = 0$, this problem has recently been studied in Ref. [25]. We here confirm and analytically explain the observations of Ref. [25] for the noninteracting case. More importantly, we also address the entanglement dynamics for finite charging energy, and reveal the underlying timescales governing this interacting case.

Before going into a detailed discussion, let us briefly

summarize the main results of our work: (i) We consider the full crossover behavior of the concurrence all the way from vanishing to large charging energy, (ii) allow for arbitrary n_g, (iii) carefully address issues related to fermion parity, (iv) include the effects of a Josephson coupling E_J to an additional bulk s-wave superconductor, (v) address the L-dependence of the concurrence by including the direct overlap ϵ_f between the MBSs, and (vi) study the timescales of entanglement generation after the sudden change of a tunnel coupling. Throughout the paper, we provide closed analytical expressions for the concurrence valid in different parameter regimes, both for the static and the time-dependent case, which are shown to give highly accurate approximations for our numerically exact results. Importantly, our results can be quantitatively interpreted in terms of an interplay of TP and CAR processes, thereby providing a comprehensive physical framework to describe entanglement in MBS devices. In contrast to Ref. [33], we provide a rather complete analysis of this problem, including both TP and CAR processes, and providing detailed analytical results for the concurrence.

The structure of this paper is as follows. In Sec. II, we briefly summarize the model for the setup in Fig. 1. For the detailed derivation of the model, we refer the reader to Refs. [30–32]. We then turn to a discussion of the entanglement-generating tunneling mechanisms in Sec. III. The concurrence, C, provides a quantitative measure for entanglement of the two dots. We compute C analytically in several parameter regimes of interest, and validate the results by comparing to exact numerical diagonalization in Sec. IV. The time-dependent concurrence obtained after a quench of tunnel couplings will then be studied in Sec. V. Finally, we offer some concluding remarks in Sec. VI. Throughout the paper, we focus on the most interesting zero-temperature limit and use units with $\hbar = 1$.

II. MODEL AND DEFINITIONS

A. Low-energy model

We start by briefly summarizing the low-energy Hamiltonian, $H = H_w + H_J + H_d + H_t$, describing the setup shown in Fig. 1, see also Refs. [30–32]. H contains (i) the part H_w for the central TS island, where a mesoscopic superconductor with charging energy E_C causes proximity-induced pairing in the nanowire, (ii) the Josephson term H_J coupling the TS island to a second bulk superconductor, (iii) the dot Hamiltonian H_d, and (iv) a tunneling Hamiltonian H_t connecting the dots and the island. We consider energy scales well below the proximity-induced superconducting gap, such that it is justified to neglect quasiparticle excitations of the TS (see also the discussion in Sec. VI). The state of the island is then fully described by specifying the integer Cooper pair number N_c on the central island, where the number operator $\hat{N}_c$

is canonically conjugate to the superconductor's phase, $[\hat{N}_c, \varphi]_- = -i$, and the occupation number n_f for the f fermion built from the MBS pair, see Eq. (1). Including the MBS hybridization (3) and a Coulomb charging term, with the single-electron charging energy E_C and a dimensionless gate-voltage parameter n_g, the island Hamiltonian is given by [30–32]

$$H_w = \epsilon_f \left(\hat{n}_f - 1/2 \right) + E_C \left(2\hat{N}_c + \hat{n}_f - n_g \right)^2, \quad (4)$$

where $\hat{n}_f = f^\dagger f$. The nonlocal f fermion representing the MBS pair thus couples to the condensate dynamics through Coulomb charging effects. Furthermore, the Josephson coupling E_J to another bulk superconductor (which is held at constant phase $\varphi_0 = 0$ and different from the superconductor responsible for the proximity-induced pairing in the nanowire) is described by

$$H_J = -E_J \cos \varphi = -\frac{E_J}{2} \left(e^{i\varphi} + e^{-i\varphi} \right), \quad (5)$$

where the operator $e^{i\varphi}$ ($e^{-i\varphi}$) raises (lowers) the Cooper pair number by one unit, $N_c \to N_c \pm 1$.

Next, each quantum dot in Fig. 1 is assumed to be in the Coulomb blockade regime such that the two dots can be modeled as single fermion levels at energies ϵ_1 and ϵ_2, see Ref. [29]. These levels can be tuned by electrostatic gates ($V_{j=1,2}$ in Fig. 1) and by the Zeeman field which induces the TS phase of the wire and also breaks spin degeneracy on the dots. As a consequence, we can use the effectively spinless fermion annihilation operator, d_j, which is connected by a tunnel coupling λ_j to γ_j, see Eq. (7) below. This tunnel coupling also captures a possible spin dependence of microscopic transition amplitudes and can be taken as real-valued positive, see Ref. [31]. The Hamiltonian describing both dots then reads

$$H_d = \sum_{j=1,2} \epsilon_j \left(\hat{n}_j - 1/2 \right), \quad (6)$$

where the number operator $\hat{n}_j = d_j^\dagger d_j$ has eigenvalues $n_j = 0, 1$. Equation (6) represents a pair of charge qubits that can be entangled through the Majorana island. While charge qubits are more susceptible to detrimental noise than spin qubits [19], it is more transparent to analyze the concurrence within the present formulation. The extension of the above model to the case of spin qubits, where local qubit operations are also easier to implement, is rather straightforward by following the route sketched in Ref. [16]. However, this case is considerably more involved on a technical level, since one then effectively needs two TS nanowires. We here discuss the simpler spinless case, but due to the spatial separation of the dots, the results reported below represent "useful entanglement" [20] that could be exploited in quantum computation schemes.

Finally, we come to the tunneling Hamiltonian H_t. Note that within our low-energy model, no TS quasiparticles are available for single-electron tunneling processes, and tunneling therefore has to involve MBSs.

We consider sufficiently large L such that d_1 is tunnel-coupled only to the MBS described by $\gamma_1 = (f + f^\dagger)/\sqrt{2}$, see Eq. (1) and Fig. 1. Similarly, the MBS coupled to d_2 corresponds to $\gamma_2 \sim f - f^\dagger$. It is now crucial to take into account charge conservation, since a floating mesoscopic superconductor cannot simply absorb or emit charge $2e$ without energy cost — this is possible only in the grounded case where $E_C = 0$. This consideration implies that tunneling terms $\sim d^\dagger f^\dagger$ must include a factor $e^{-i\varphi}$, which annihilates a Cooper pair and thus restores charge balance. With the gauge choice in Ref. [31], we obtain

$$H_t = \frac{1}{\sqrt{2}} \sum_{j=1,2} \lambda_j d_j^\dagger \left[f + (-)^{j-1} e^{-i\varphi} f^\dagger \right] + \text{H.c.,} \quad (7)$$

where "normal" tunneling terms like $d^\dagger f$ do not affect the condensate but "anomalous" tunneling terms such as $d^\dagger e^{-i\varphi} f^\dagger$ change the Cooper pair number by one unit.

In what follows, it will be convenient to choose occupation number basis states,

$$|n_1 n_2 n_f, N_c\rangle = \left(d_1^\dagger \right)^{n_1} \left(d_2^\dagger \right)^{n_2} \left(f^\dagger \right)^{n_f} |000, N_c\rangle, \quad (8)$$

to represent the Hamiltonian. For this basis choice, the quantum numbers take the values $n_{1,2,f} = 0, 1$ and $N_c = -N_{\max}, \ldots, N_{\max}$, where $N_{\max}$ restricts the number of Cooper pairs. Here $N_{\max}$ is taken relative to $n_g/2$, and the $N_{\max} \to \infty$ limit of interest is rapidly approached when E_C is finite. The basis size is then $2M = 8(2N_{\max} + 1)$, and H becomes a $2M \times 2M$ matrix. Diagonalization of this matrix yields the ground state $|\Psi\rangle$, which in turn determines the amount of entanglement between the two dots as explained below.

B. Concurrence

In order to quantify entanglement, one has to identify a suitable measure. For our bipartite case with two single-level quantum dots, a convenient and reliable measure is given by the concurrence, even though its construction is rather formal and abstract [20]. The concurrence is expressed in terms of the reduced density matrix ρ_d for the dots, which follows from the full density matrix after tracing over the island degrees of freedom. In the zero temperature limit, this yields the Hermitian 4×4 matrix

$$\rho_d = \text{Tr}_{n_f, N_c} |\Psi\rangle\langle\Psi|, \quad (9)$$

with trace equal to unity. The concurrence is then defined by [20]

$$C = \max\left(0, \sqrt{\lambda_1} - \sqrt{\lambda_2} - \sqrt{\lambda_3} - \sqrt{\lambda_4} \right), \quad (10)$$

with the eigenvalues $\lambda_1 \geq \lambda_2 \geq \lambda_3 \geq \lambda_4$ of the matrix

$$G = \rho_d (\sigma_y \otimes \sigma_y) \rho_d^* (\sigma_y \otimes \sigma_y), \quad (11)$$

where ρ_d^* denotes the complex conjugate of ρ_d and the σ_y Pauli matrices act in the respective $|n_j\rangle$ (with $n_j = 0, 1$) space corresponding to each of the two dots. Equation (10) implies $0 \leq C \leq 1$, with $C = 0$ for separable (non-entangled) states and $C = 1$ for maximally entangled states. We note that the concurrence defined in Eq. (10) is a gauge-invariant quantity, i.e., we can use the above gauge choice with real-valued λ_j in Eq. (7).

We have also computed the negativity [20], which is an alternative measure for entanglement. While detailed results for the negativity differ from those for the concurrence, the physical conclusions are the same. From now on, we therefore discuss the concurrence only. Numerically, C follows from Eq. (10) once the full ground state of the total system, $|\Psi\rangle$, has been determined by diagonalization of the $2M \times 2M$ Hamiltonian matrix.

Analytical progress is possible when $|\Psi\rangle$ has a simple form. An important example is given by

$$|\Psi\rangle = c_1|000, N_1\rangle + c_2|011, N_2\rangle + c_3|101, N_3\rangle + c_4|110, N_4\rangle, \quad (12)$$

with arbitrary Cooper pair numbers N_j and complex coefficients c_j subject to normalization, $\sum_{j=1}^4 |c_j|^2 = 1$. Calculating C in Eq. (10) for this state, we find that at least one pair of number states in Eq. (12) must have identical (n_f, N_c) in order to produce entanglement. There are two such possibilities, (i) $N_1 = N_4$ with $|c_1 c_4| \geq |c_2 c_3|$, or (ii) $N_2 = N_3$ with $|c_2 c_3| \geq |c_1 c_4|$. In both cases, the concurrence is given by

$$C = 2\left||c_1 c_4| - |c_2 c_3|\right|, \quad (13)$$

see also Ref. [33]. Suppressing the (n_f, N_c) indices, maximally entangled states with $C = 1$ thus correspond to the Bell states

$$|\Phi_A\rangle = \frac{1}{\sqrt{2}} \left(|01\rangle + e^{i\phi_A}|10\rangle \right), \quad (14)$$

$$|\Phi_B\rangle = \frac{1}{\sqrt{2}} \left(|00\rangle + e^{i\phi_B}|11\rangle \right),$$

with arbitrary phases $\phi_{A/B}$.

C. Parity conservation and symmetry relations

Let us now address symmetries and conserved quantities for our model. We first note that the total fermion parity defined as

$$\mathcal{P} = (-1)^{n_1 + n_2 + n_f} \quad (15)$$

is a conserved quantity since H contains no terms mixing states with even and odd total electron number. The even-parity (odd-parity) sector has $\mathcal{P} = +1$ ($\mathcal{P} = -1$), where the parity-resolved ground states, $|\Psi, \mathcal{P}\rangle$, follow by diagonalization of a Hamiltonian matrix of size $M \times M$ only. Conservation of $\mathcal{P}$ will generally be weakly broken in concrete physical realizations due to quasiparticles neglected in our model. In the presence of parity relaxation,

the true ground state then corresponds to the $|\Psi, \mathcal{P}\rangle$ state with lower energy. However, we here assume that $\mathcal{P}$ is conserved on all timescales of interest, such that both states $|\Psi, \mathcal{P}\rangle$ are experimentally relevant and the concurrence depends on total fermion parity, $C = C_{\mathcal{P}}$. Although this assumption represents an experimental challenge due to the inevitable presence of residual quasiparticle poisoning, very recent experiments indicate that the corresponding timescales may reach minutes in similar devices as considered here [45, 46].

We now turn to the n_g-dependence of the parity-constrained concurrence, $C_{\mathcal{P}}(n_g)$. Since a shift $n_g \rightarrow n_g + 2$ can be absorbed by shifting $N_c \rightarrow N_c + 1$ in the Hamiltonian, see Eq. (4), all observables have to be periodic in n_g with period $\Delta n_g = 2$. (In the presence of parity relaxation, the period will in general be reduced to $\Delta n_g = 1$.) We thus obtain a first symmetry relation for the concurrence,

$$C_{\mathcal{P}}(n_g) = C_{\mathcal{P}}(n_g + 2). \qquad (16)$$

This relation allows us to restrict n_g to the window $0 \leq n_g < 2$ throughout.

A second relation follows from an electron-hole-like symmetry property of H which relates the odd- and even-parity concurrences,

$$C_{\mathcal{P}}(n_g; \epsilon_1, \epsilon_2, \epsilon_f) = C_{-\mathcal{P}}(1 - n_g; -\epsilon_1, -\epsilon_2, -\epsilon_f). \quad (17)$$

In order to derive Eq. (17), we first note that H is invariant under the replacement $\epsilon_{1,2,f} \rightarrow -\epsilon_{1,2,f}$ with $n_g \rightarrow 1 - n_g$, accompanied by a "particle-hole transformation" U that exchanges creation and annihilation operators, $f \leftrightarrow f^\dagger$ etc., and $e^{i\varphi} \rightarrow e^{-i\varphi}$ yielding $N_c \rightarrow -N_c$. This symmetry implies that if we have the ground state $|\Psi(\epsilon_{1,2,f}, n_g)\rangle$, we obtain another ground state from the relation

$$|\Psi(-\epsilon_{1,2,f}, 1 - n_g)\rangle = U|\Psi(\epsilon_{1,2,f}, n_g)\rangle. \qquad (18)$$

Now the point is that these two ground states have different total parities. Indeed, the original state has $\mathcal{P} = (-1)^{n_1 + n_2 + n_f}$, while the transformed one has $\mathcal{P}' = (-1)^{(1-n_1)+(1-n_2)+(1-n_f)} = -\mathcal{P}$. We thus arrive at Eq. (17). In passing we note that for an island hosting more than one pair of MBSs, if an odd number of dots is tunnel-coupled to MBSs, we instead would have $\mathcal{P}' = \mathcal{P}$, and Eq. (17) does not connect different parity sectors anymore. Moreover, the above arguments also show that the relative sign between N_c and n_f in Eq. (4) is irrelevant.

For our island with a single MBS pair, Eq. (17) states that the concurrence in the odd-parity sector directly follows from the even-parity result by simply inverting the energy scales $\epsilon_{1,2,f}$ and letting $n_g \rightarrow 1 - n_g$. From now on, unless noted otherwise, we therefore describe results for the even-parity sector $\mathcal{P} = +1$ only, where it is sufficient to consider gate-voltage parameters in the window $0 \leq n_g < 2$.

III. ENTANGLEMENT-GENERATING PROCESSES

Before turning to detailed results for the concurrence of the two dots in Fig. 1, let us first discuss the entanglement-generating processes at work in such a system, where the nonlocality of the f fermion built from the MBS pair turns out to be crucial. When searching for maximally entangled states of the two dots, Eq. (14) suggests two candidate sets for suitable superpositions of dot states $|n_1 n_2\rangle$,

$$A = \{|10\rangle, |01\rangle\}, \qquad B = \{|00\rangle, |11\rangle\}. \qquad (19)$$

In this section, we shall focus on the large-E_C case, assuming that n_g is not half-integer such that the equilibrium island state is uniquely defined. Hence the Cooper pair number corresponds to $N_c = 0$, and for $\mathcal{P} = +1$, we have $n_f = 1$ ($n_f = 0$) for set A (B).

To realize the maximally entangled Bell states (14), (virtual) tunneling processes through the island now have to provide the necessary coupling between states within a given set. The resulting superpositions should ideally have equal weight, which is possible when the dot energy levels are adjusted to fulfill the condition $\epsilon_1 = \epsilon_2$ ($\epsilon_1 = -\epsilon_2$) for states in set A (B). Perturbation theory in the tunneling amplitudes then shows the existence of two different entanglement-generating mechanisms, namely elastic cotunneling (i.e., TP) and CAR. In fact, our quantitative results will find a natural interpretation in terms of these two mechanisms.

A. Teleportation

The TP mechanism refers to the nonlocal transfer of an electron across the TS island. For example, let us consider the state $|10\rangle$, where an electron resides in the left dot and the right dot is empty. We now study how a coupling to the partner state $|01\rangle$ in set A is established by H_t. After the in-tunneling process from the left dot, the island charge will change by one unit. However, this change typically comes with an energy cost of order E_C and, therefore, is possible only as a virtual process. The corresponding out-tunneling event restores the equilibrium charge state again and thereby may transfer an electron to the right dot. In effect, this process is similar to elastic cotunneling [19] but with two major differences. First, TP has a highly nonlocal character inherited from the nonlocality of the f fermion. Second, because of the existence of "normal" and "anomalous" tunneling terms in H_t, there are two different contributions. Using the notation in Eq. (8), the first one (denoted by TP_n) proceeds solely by "normal" tunneling ($\sim d^\dagger f, f^\dagger d$), while the second contribution (TP_a) only employs "anomalous" tunneling processes,

$$\mathrm{TP}_n : |101, 0\rangle \xrightarrow{\lambda_2} |110, 0\rangle \xrightarrow{\lambda_1} |011, 0\rangle, \qquad (20)$$

$$\mathrm{TP}_a : |101, 0\rangle \xrightarrow{\lambda_1} |000, 1\rangle \xrightarrow{\lambda_2} |011, 0\rangle.$$

By virtue of the processes in Eq. (20), the $|10\rangle$ and $|01\rangle$ states are coupled together. For $\epsilon_1 = \epsilon_2$, both states enter the superposition with equal weight. They may then form the maximally entangled Bell state $|\Phi_A\rangle$ in Eq. (14), where TP is responsible for long-range entanglement.

Finally, we note that the TP phenomenon discussed by Fu [30] is a resonant version of the above process, which takes place near half-integer values of n_g. We will address this case in detail in Sec. IV A, where we show that perfect entanglement is not possible under Coulomb blockade peak conditions.

B. Crossed Andreev reflection

CAR provides a distinct second entanglement-generating mechanism, where for $\epsilon_1 = -\epsilon_2$, the two dot states in set B enter the superposition with equal weight and may yield the Bell state $|\Phi_B\rangle$ in Eq. (14). Since entangled states have to involve a pair of number states with matching (n_f, N_c) entries, see Eq. (13), the two states of interest now correspond to $|000, 0\rangle$ and $|110, 0\rangle$. Their total particle numbers are different, and hence not only the tunnel couplings $\lambda_{1,2}$, but also a finite Josephson coupling E_J to another bulk superconductor is needed in order to yield non-zero concurrence. We now show that this condition arises even though CAR processes can connect states with different island particle number $2N_c + n_f$ already for $E_J = 0$. Indeed, starting from $|000, 0\rangle$, there are six different CAR transitions corresponding to all permutations of the three elementary transfer processes $\sim \lambda_1, \lambda_2, E_J$. As an example, we show two of these CAR sequences,

$$\text{CAR}_1 : |000, 0\rangle \xrightarrow{\lambda_2} |011, -1\rangle \xrightarrow{E_J} |011, 0\rangle \xrightarrow{\lambda_1} |110, 0\rangle,$$
$$\text{CAR}_2 : |000, 0\rangle \xrightarrow{E_J} |000, 1\rangle \xrightarrow{\lambda_1} |101, 0\rangle \xrightarrow{\lambda_2} |110, 0\rangle,$$
$$(21)$$

where the first (second) step for the CAR_1 (CAR_2) process describes anomalous tunneling, the respective third step corresponds to normal tunneling, and the second (first) step involves the Josephson coupling in Eq. (5). In the latter step, a Cooper pair is transferred to the TS island. It is only because of this step that the two states $|000, 0\rangle$ and $|110, 0\rangle$ can be connected. Finally, we note that in our quantitative analysis below, not only the two processes in Eq. (21) but all six CAR sequences will be taken into account.

IV. MBS-MEDIATED ENTANGLEMENT

In this section, we quantitatively discuss the concurrence C, describing the amount of entanglement between the two dots in Fig. 1, by comparing analytical expressions in different parameter regimes to the corresponding numerically exact results obtained from the ground state of the full system, see Eq. (10). Since the entire

behavior of the concurrence in the odd-parity sector follows from the even-parity results, see Eq. (17), we shall only discuss the case $\mathcal{P} = +1$. Furthermore, because of Eq. (16), the gate parameter n_g can be taken in the window $0 \leq n_g < 2$.

For convenience, we will employ a compact notation for the number states by writing $|\nu\rangle = |n_1 n_2 n_f, N_c\rangle$ in Eq. (8). Without the Josephson coupling and the tunnel amplitudes, i.e., for $E_J = \lambda_{1,2} = 0$, the eigenenergies of the full system are then given by

$$E_\nu = E_C(Q - n_g)^2 + \sum_{j=1,2,f} \epsilon_j(n_j - 1/2), \qquad (22)$$

with the integer island particle number $Q = 2N_c + n_f$. The dependence of E_ν on Q includes the well-known Coulomb charging energy parabola [19] and is sketched in Fig. 2. We shall return to Fig. 2 below when discussing our analytical results for the concurrence. Moreover, the symbol $\mathcal{N}$ appearing in some equations below denotes a normalization constant for the respective state.

Before describing our results for the concurrence in detail, we pause to offer some guidance for focused readers. In Sec. IV A, we analyze the limit of strong Coulomb blockade, where the charging energy is the dominant energy scale and only a few island charge states are accessible. We derive analytical expressions for the concurrence C for gate-voltage parameters near the Coulomb blockade valleys centered around $n_g = 1$, see Eq. (30), and $n_g = 0 \mod 2$, see Eq. (36) below. In addition, we also provide closed results valid near a Coulomb blockade peak, see Eq. (42), and compare our analytical results to full numerical diagonalization. We then briefly discuss the noninteracting ($E_C = 0$) limit in Sec. IV B, where the concurrence follows as given in Eq. (48). Finally, we return to the strong-E_C limit in Sec. IV C but now also allow for a strong MBS hybridization ϵ_f, i.e., arbitrary length L in Eq. (3). However, for simplicity, we only study the case of integer n_g in Sec. IV C.

A. Strong Coulomb blockade regime

We start our quantitative analysis of the concurrence with the limit of large E_C,

$$E_C \gg \max|\epsilon_{1,2,f}, \lambda_{1,2}, E_J|, \qquad (23)$$

where the charging energy dominates over all other energy scales except for the TS gap, which implicitly sets the ultraviolet cutoff for our model. The parameter regime in Eq. (23) has also been addressed in Refs. [33, 34]. It is convenient to distinguish four different, partially overlapping, gate-voltage parameter windows defined by

$$n_g = n_{g,0} + \eta/2, \quad n_{g,0} \in \left\{0, \frac{1}{2}, 1, \frac{3}{2}\right\}, \qquad (24)$$
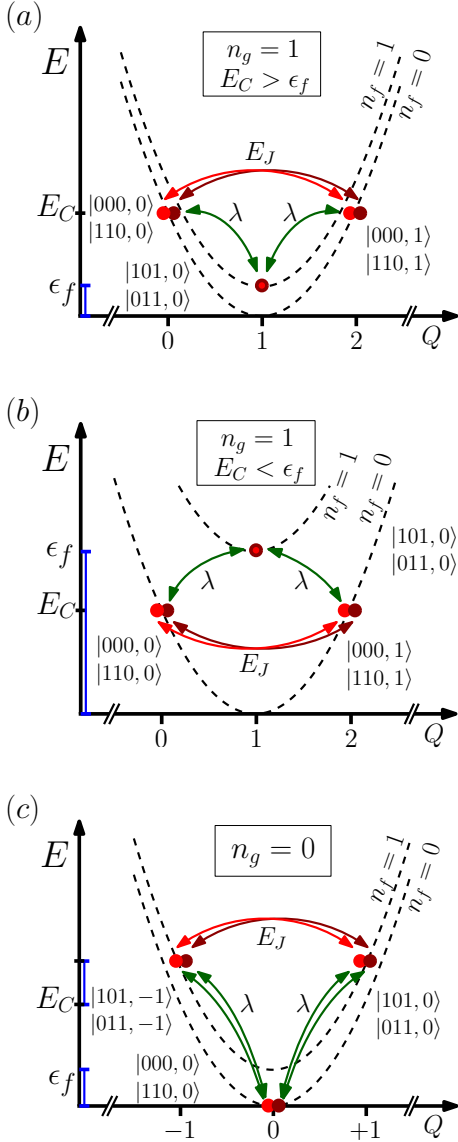
Figure 2. Schematic illustration of the energy E_ν, see Eq. (22), vs the island particle number $Q = 2N_c + n_f$ for $\epsilon_{1,2} = 0$. Panel (a) shows the case $n_g = 1$ for $E_C > \epsilon_f$. Panel (b) is also for $n_g = 1$ but with $E_C < \epsilon_f$, while panel (c) is for $n_g = 0$. The respective even-parity states $|\nu\rangle = |n_1 n_2 n_f, N_c\rangle$ are also indicated, where tunneling ($\lambda \neq 0$) and/or Josephson ($E_J \neq 0$) processes cause the shown transitions.

where $|\eta| < 1$ parametrizes the deviation from the respective center value $n_g = n_{g,0}$. For both half-integer values of $n_g = n_{g,0}$, the dominant charging energy contribution, given by the first term in Eq. (22), is precisely degenerate and thus corresponds to a Coulomb blockade conductance peak [32]. We present our results for this case later on, but first turn to the Coulomb blockade valley at $n_{g,0} = 1$.

Coulomb blockade valley near $n_g = 1$

For $n_{g,0} = 1$ in Eq. (24), we observe from Fig. 2(a) that the ground state has island occupation number $Q = 1$ in order to minimize the large Coulomb energy, such that $n_f = 1$ and $N_c = 0$. For $\mathcal{P} = +1$, one additional electron then has to occupy the dots. As a consequence, the low-energy sector is spanned by

$$\mathcal{H}_0 = \{|101,0\rangle, |011,0\rangle\}, \qquad (25)$$

with the two states denoted by $|\nu_0\rangle$. The energetically closest set of states, $|\nu_1\rangle \in \mathcal{H}_1$, has $Q = 0$ or $Q = 2$, see Fig. 2(a), where the f-electron level representing the MBS pair is empty, $n_f = 0$, with $N_c = 0$ or $N_c = 1$. The two dots are then either both occupied or both empty, resulting in the subspace

$$\mathcal{H}_1 = \{|000,0\rangle, |110,0\rangle, |000,1\rangle, |110,1\rangle\}. \qquad (26)$$

These states are separated from the $\mathcal{H}_0$ sector by an energy of order E_C. This separation of energy scales allows us to derive a low-energy Hamiltonian, $\tilde{H}$, describing the parameter regime in Eq. (23) for gate-voltage parameters close to $n_{g,0} = 1$. This reduced Hamiltonian is obtained by projecting the full Hamiltonian to the subspace $\mathcal{H}_0$ only. Using the two basis states $|\nu_0\rangle$ in Eq. (25), $\tilde{H}$ corresponds to a 2×2 matrix, such that it is straightforward to determine the ground state and the concurrence analytically.

The above projection is implemented by disregarding all high-energy states beyond $|\nu_1\rangle \in \mathcal{H}_1$ in Eq. (26) and by treating the coupling between the subspaces $\mathcal{H}_0$ and $\mathcal{H}_1$ through a Schrieffer-Wolff transformation [39, 47], which here is equivalent to second-order perturbation theory. For $E_C > \epsilon_f$, this coupling is due to tunneling (H_t) only, see Fig. 2(a), and with the energies E_ν in Eq. (22), we obtain

$$\tilde{H} = \sum_{\nu_0} E_{\nu_0} |\nu_0\rangle\langle\nu_0| + \frac{1}{2} \sum_{\nu_0,\nu_0'} |\nu_0\rangle\langle\nu_0'| \qquad (27)$$

$$\times \sum_{\nu_1} \left(\frac{1}{E_{\nu_0} - E_{\nu_1}} + \frac{1}{E_{\nu_0'} - E_{\nu_1}} \right) \langle\nu_0|H_t|\nu_1\rangle\langle\nu_1|H_t|\nu_0'\rangle,$$

where the second term describes virtual excursions to the energetically higher $|\nu_1\rangle$ states. Using Eq. (23), $\epsilon_{1,2,f}$-terms in the respective denominators are small against the large charging energy contribution, and up to an overall energy shift, we arrive at

$$\tilde{H} = \begin{pmatrix} a & b \\ b & -a \end{pmatrix}, \qquad (28)$$

$$a = \frac{\epsilon_1 - \epsilon_2}{2} - \frac{\eta(\lambda_1^2 - \lambda_2^2)}{2E_C(1-\eta^2)},$$

$$b = \frac{\lambda_1 \lambda_2}{E_C(1-\eta^2)},$$

where η parametrizes n_g around $n_{g,0} = 1$, see Eq. (24). The ground state of Eq. (28) is

$$|\Psi\rangle = \mathcal{N}\left[\left(a - \sqrt{a^2 + b^2}\right)|101,0\rangle + b|011,0\rangle \right], \qquad (29)$$

which matches the general form in Eq. (12). The concurrence then directly follows from Eq. (13),

$$C(X_1) = \frac{1}{\sqrt{1 + X_1^2}}, \quad X_1 = \frac{a}{b}, \qquad (30)$$

stating that C is a universal function of a single parameter X_1 which depends on basically all the microscopic parameters according to Eq. (28).

For $X_1 = 0$, Eq. (30) yields the ideal value, $C = 1$, characterizing perfect entanglement. Indeed, Eq. (29) then reduces to the Bell state $|\Phi_A\rangle$ in Eq. (14), and we conclude that entanglement is here established by the TP mechanism. This condition for perfect entanglement is fulfilled for all symmetric systems, i.e., for identical dot level energies and tunneling strengths,

$$\epsilon_1 = \epsilon_2 = \epsilon, \quad \lambda_1 = \lambda_2 = \lambda. \qquad (31)$$

The approximations leading to the reduced Hamiltonian (28), and hence to the concurrence in Eq. (30), eventually break down near a Coulomb peak with $|\eta| \to 1$. Nonetheless, Eq. (30) shows that $C = 1$ can persist over an extended gate-voltage parameter window around $n_{g,0} = 1$.

Coulomb blockade valley near $n_g = 0$

In a similar manner, we next study what happens around $n_{g,0} = 0$. In Fig. 2(c), we show a subset of the relevant states, implementing two of the possible six CAR processes. The energy E_ν is then minimized for $n_f = N_c = 0$, and the $\mathcal{P} = +1$ low-energy sector is spanned by

$$\mathcal{H}_0^{(n_{g,0}=0)} = \{|000, 0\rangle, |110, 0\rangle\}, \qquad (32)$$

where both dot levels are either occupied or empty. The excited states relevant for CAR processes, cf. Sec. III B, then correspond to

$$\mathcal{H}_1^{(n_{g,0}=0)} = \{|110, -1\rangle, |101, -1\rangle, |011, -1\rangle,$$
$$|101, 0\rangle, |011, 0\rangle, |000, 1\rangle\}, \qquad (33)$$

where the first and the last state have island charge $Q = \mp 2$ and thus are highest in energy, $\sim 4E_C$, while the remaining states (with $Q = \pm 1$) are separated from the $\mathcal{H}_0$ sector by an energy scale $\sim E_C$.

The two states in Eq. (32) have different total particle number. As discussed in Sec. III B, see also Fig. 2(c), the CAR mechanism connecting those states has to involve a finite Josephson coupling E_J and therefore constitutes a third-order process. In particular, now a transition within the high-energy sector in Eq. (33) is necessary, and we thus have to include one normal tunneling, one anomalous tunneling, and one Josephson process, i.e., we have to apply H_t twice and H_J once, see Eqs. (7) and (5). The corresponding third-order perturbation theory can again be implemented by a Schrieffer-Wolff transformation [47], which effectively yields $\tilde{H} \to \tilde{H} + H^{(3)}$ for the

reduced Hamiltonian in Eq. (27). With $\tilde{H}_t = H_t + H_J$, we find [48]

$$H^{(3)} = \sum_{\nu_0, \nu_0', \nu_1, \nu_1'} \frac{\langle \nu_0|\tilde{H}_t|\nu_1\rangle\langle \nu_1|\tilde{H}_t|\nu_1'\rangle\langle \nu_1'|\tilde{H}_t|\nu_0'\rangle}{(E_{\nu_0} - E_{\nu_1})(E_{\nu_0} - E_{\nu_1'})}|\nu_0\rangle\langle\nu_0'|, \qquad (34)$$

where $|\nu_1\rangle$ and $|\nu_1'\rangle$ are the virtually occupied higher-energy states in Eq. (33) and terms $\sim \epsilon_{1,2,f}$ are small against the charging energy contributions in the denominator. Using the two states in Eq. (32) to represent $\tilde{H}$, we obtain the same 2×2 matrix as in Eq. (28) but with the replacements

$$a \to a' = -\frac{\epsilon_1 + \epsilon_2}{2} + \frac{\eta(\lambda_1^2 + \lambda_2^2)}{2E_C(1 - \eta^2)}, \qquad (35)$$
$$b \to b' = -\frac{3\lambda_1\lambda_2 E_J}{E_C^2(1 - \eta^2)(4 - \eta^2)},$$

where η now parametrizes n_g around $n_{g,0} = 0$. We observe that second-order processes only give corrections to the state energies (a'), while third-order CAR processes produce the crucial coupling of both states (b') needed for entanglement. We note in passing that second-order corrections $\sim E_J^2$ only give an irrelevant constant energy shift that has been dropped in Eq. (35). The ground state finally follows as in Eq. (29), but with the basis states in Eq. (32) and the replacements in Eq. (35). Hence the concurrence is again given by Eq. (30) but with $X_1 \to X_0 = a'/b'$.

Although these results look very similar, there are crucial differences in the entanglement properties when compared to the $n_{g,0} = 1$ case. In particular, although we may have $X_0 = 0$ for a specific gate-voltage parameter (η), such that perfect entanglement is realized, it is not possible to have $C = 1$ over a wide parameter range anymore. In that sense, within the large-E_C regime defined in Eq. (23), entanglement produced by the CAR mechanism is less stable than the one caused by TP. To demonstrate this point, consider dot energies $\epsilon_1 = -\epsilon_2$ where CAR processes are most effective, cf. Sec. III B, keeping symmetric tunnel couplings as before, $\lambda_1 = \lambda_2 = \lambda$. We then obtain

$$C(X_0) = \frac{1}{\sqrt{1 + X_0^2}}, \quad X_0 = -\frac{(4 - \eta^2)\eta E_C}{3E_J}, \qquad (36)$$

describing a narrow concurrence peak centered around $n_g = 0$, with height $C(0) = 1$ and width $\delta n_g \sim E_J/E_C$. This concurrence peak is a clear signature of CAR processes and can easily be distinguished from the broad and robust $C = 1$ plateau generated by TP around $n_g = 1$. In particular, the CAR entanglement peak quickly disappears with increasing $|\epsilon_1 + \epsilon_2|$, while it remains stable against variations with $\epsilon_1 \approx -\epsilon_2$. We thus obtain precisely the opposite behavior as for the TP-generated concurrence plateau.

Concurrence near Coulomb blockade peaks

Next we study the concurrence behavior near half-integer values of n_g. For simplicity, we discuss the most interesting symmetric case defined in Eq. (31). With n_g near $n_{g,0} = 1/2$, there are four low-energy states corresponding to the subspace

$$\mathcal{H}_0^{(n_{g,0}=1/2)} = \{|000,0\rangle, |110,0\rangle, |101,0\rangle, |011,0\rangle\}. \quad (37)$$

Since these states are already directly coupled by tunneling, the reduced Hamiltonian $\tilde{H}$ can simply be obtained by projecting H to the subspace in Eq. (37), thereby neglecting all virtual excursions to higher energy states. When represented in the basis (37), up to an irrelevant overall constant, $\tilde{H}$ then takes the form

$$\tilde{H}^{(n_{g,0}=1/2)} = \begin{pmatrix} \tilde{E} - 2\epsilon & 0 & 0 & 0 \\ 0 & \tilde{E} & \lambda/\sqrt{2} & -\lambda/\sqrt{2} \\ 0 & \lambda/\sqrt{2} & -\tilde{E} & 0 \\ 0 & -\lambda/\sqrt{2} & 0 & -\tilde{E} \end{pmatrix}, \quad (38)$$

with the n_g-dependent energy scale

$$\tilde{E} = E_C(n_g - 1/2) + (\epsilon - \epsilon_f)/2. \quad (39)$$

The ground state of $\tilde{H}$ is either given by

$$|\Psi_1\rangle = \mathcal{N}\Big[\Big(\sqrt{\tilde{E}^2 + \lambda^2} - \tilde{E}\Big)|110,0\rangle \quad (40)$$
$$- \frac{\lambda}{\sqrt{2}}|101,0\rangle + \frac{\lambda}{\sqrt{2}}|011,0\rangle\Big],$$

or it corresponds to the separable $C = 0$ state $|\Psi_2\rangle = |000,0\rangle$. The respective energies are

$$E_1 = -\sqrt{\tilde{E}^2 + \lambda^2}, \quad E_2 = \tilde{E} - 2\epsilon. \quad (41)$$

Since $|\Psi_1\rangle$ is of the form in Eq. (12), we can again use Eq. (13) to directly read off the concurrence, but $E_2 > E_1$ is necessary to have a finite concurrence. With the Heaviside step function Θ, we thus obtain the concurrence in analytical form,

$$C(\tilde{E}/\lambda, \epsilon/\lambda) = \frac{\Theta(E_2 - E_1)}{1 + \left[\left(\sqrt{\tilde{E}^2 + \lambda^2} - \tilde{E}\right)/\lambda\right]^2}, \quad (42)$$

which now depends on two parameters. In order to obtain a non-zero value in Eq. (42), the gate parameter must be above a critical value, $n_g > n_0$, with

$$n_0 = \frac{1}{2} + \frac{\epsilon_f + \epsilon}{2E_C} - \frac{\lambda^2}{4\epsilon E_C}. \quad (43)$$

This relation is only relevant when $\epsilon > 0$, since the condition $E_2 > E_1$ is always met for $\epsilon \leq 0$. For $\epsilon > 0$, the concurrence thus exhibits an abrupt jump from $C = 0$ to a finite value as n_g increases through n_0.

On the other hand, it can happen that at some gate parameter $n_g^{(C=1/2)}$ (above n_0 for $\epsilon > 0$), the turnover value $C = 1/2$ separating the CAR-dominated regime (near the $n_g = 0$ valley) from the TP-dominated regime (near $n_g = 1$) is reached. Using Eq. (42), this point is at $\tilde{E} = 0$, corresponding to

$$n_g^{(C=1/2)} = \frac{1}{2} + \frac{\epsilon_f - \epsilon}{2E_C}. \quad (44)$$

Note that this expression holds in particular for $\epsilon \leq 0$. We therefore see that the gate parameter $n_{g,c}$ determining the transition through $C = 1/2$ is given by

$$n_{g,c} = \max\left(n_0, n_g^{(C=1/2)}\right) \simeq \frac{1}{2} + \frac{\epsilon_f + |\epsilon|}{2E_C}, \quad (45)$$

where the last expression becomes exact for $\lambda \ll |\epsilon|$. For $n_0 > n_g^{(C=1/2)}$, the concurrence transition is an abrupt jump. Otherwise, it is a smooth transition, and the concurrence jump only happens at a gate parameter $n_g = n_0 < n_g^{(C=1/2)}$ where C has already dropped to a small value.

The actual value for $n_{g,c}$ in Eq. (45) is close to $n_g = 1/2$ for large E_C, but it exhibits a systematic shift towards $n_g = 1$ when $|\epsilon|$ increases. We also note that as n_g moves from $n_{g,c}$ towards $n_g = 1$, the concurrence given by Eq. (42) approaches the perfect entanglement regime, $C \to 1$, as predicted by our expansion around $n_g = 1$. Consequently, our results for $C(n_g)$ obtained within different n_g windows smoothly match onto each other.

Finally, a similar analysis can be carried out for n_g near $n_{g,0} = 3/2$. The result is given by Eq. (42) again but with the replacements $n_g \to 2 - n_g$ and $\epsilon \to -\epsilon$. For $\lambda \lesssim |\epsilon|$, the transition corresponding to Eq. (45) now takes place at the gate parameter

$$n_{g,c} \simeq \frac{3}{2} - \frac{\epsilon_f + |\epsilon|}{2E_C}, \quad (46)$$

which again shifts towards $n_g = 1$ with increasing $|\epsilon|$.

Discussion

With analytical results for the concurrence at our disposal, we now compare them to numerically exact results. The n_g-dependence of the concurrence for $\epsilon_f = E_J = 0$ is shown in Fig. 3, where we consider a symmetric system with $\epsilon = 0$. For $E_C = 20\lambda$, the analytical curve almost perfectly matches the numerically exact result, where we have $C = 1$ for practically the full valley range $1/2 < n_g < 3/2$, with a sharp crossover around $n_g = 1/2$ to $C = 0$ near even n_g. For $E_C = 5\lambda$, the qualitative behavior is still captured by our analytical expressions but there are quantitative differences, as expected when moving away from the strong-E_C limit. We note in passing that for odd parity, the concurrence behavior in both valleys will effectively be interchanged.
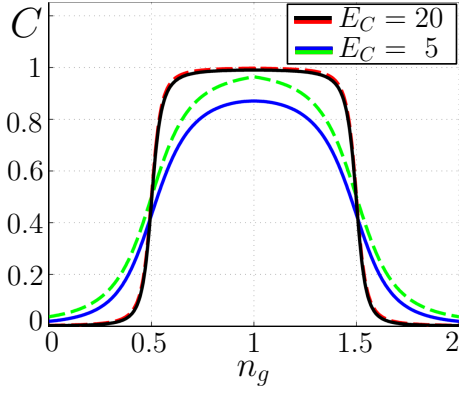
Figure 3. Concurrence C vs n_g for the even-parity sector with $\epsilon_f = E_J = 0$. We consider a symmetric system, see Eq. (31), with $\epsilon = 0$ and $\lambda = 1$, for two different values of E_C. Solid curves are obtained by numerical diagonalization of the full model. Dashed curves represent the analytical result derived in the large-E_C limit, see Eqs. (30) and (42). With $C(n_g) = C(n_g + 2)$, see Eq. (16), we only show one period.
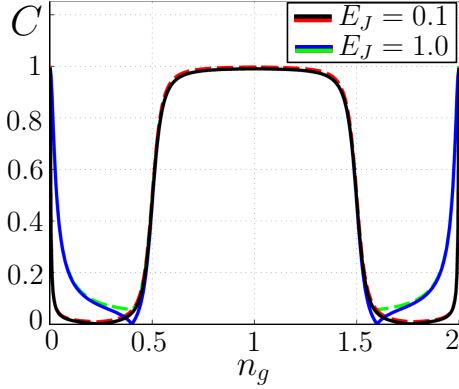

Figure 4. Same as Fig. 3 but for finite E_J and $E_C = 20$. The dashed curves again give analytical results, using Eq. (36) near $n_g = 0$ and $n_g = 2$.

Let us next address the effects of adding a small but finite Josephson coupling E_J, where we again study a symmetric system with $\epsilon = \epsilon_f = 0$. The concurrence is shown in Fig. 4 for $E_C = 20\lambda$. We first notice that near $n_g = 1$, the effects of E_J are negligible and the TP-induced perfect value $C = 1$ is robust against adding a small Josephson coupling. However, we now encounter the predicted narrow concurrence peak with width $\delta n_g \sim E_J/E_C$ centered at $n_g = 0 \bmod 2$, see Eq. (36), which provides a very characteristic signature of CAR processes.

In Figs. 3 and 4, we have considered a symmetric system with $\epsilon = \epsilon_f = 0$, where the concurrence exhibits the additional symmetry $C(n_g) = C(2 - n_g)$, and the turnover between both concurrence regimes is perfectly smooth and happens precisely at half-integer n_g. However, both of these features will not be present in general, and a counter-example with finite ϵ is shown in Fig. 5. In accordance with Eqs. (45) and (46), we find that the turnover points between the CAR- and TP-dominated
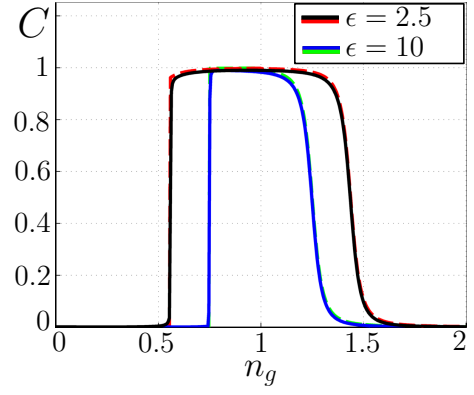

Figure 5. Same as Fig. 4 but for finite ϵ, using $E_J = 1$.

regimes move closer to $n_g = 1$ with increasing ϵ. As expected from our above discussion, we also confirm that for $\epsilon > 0$, the crossover in $C(n_g)$ (at n_g slightly above $n_g = 1/2$) deforms into an abrupt jump, while the corresponding crossover near $n_g = 3/2$ stays smooth. Hence Fig. 5 clearly shows that $C(n_g) \neq C(2 - n_g)$. We mention in passing that for finite but very small ϵ, the narrow entanglement peak seen in Fig. 4 may survive, but with the center position shifted to finite n_g. However, this peak is found to quickly disappear with increasing $|\epsilon|$, cf. Sec. III B, and is altogether absent for the parameters in Fig. 5.

B. Noninteracting case

Let us now briefly address the noninteracting case, $E_C = 0$, where the Cooper pair sector decouples from the fermionic sector spanned by the $|n_1 n_2 n_f\rangle$ states. The $E_C = 0$ case with normal metallic leads instead of our dots was studied in Ref. [23], while the dot case was also considered in Ref. [25]. An alternative way to reach the noninteracting limit is to let $E_J \to \infty$, where all $|N_c\rangle$ states are strongly mixed and charge quantization effects are washed out [32]. In both limits, $E_C \to 0$ or $E_J \to \infty$, one arrives at the same effective Hamiltonian $\tilde{H}$, where the parameters E_C, n_g and E_J do not appear anymore.

In the even-parity sector, $\tilde{H}$ has a 4×4 matrix representation, which can easily be diagonalized to yield the ground state $|\Psi\rangle$. For the symmetric case with $\epsilon = 0$, see Eq. (31), and omitting the redundant N_c indices, we find

$$|\Psi\rangle = \mathcal{N}\Big\{ \Big(\epsilon_f + \sqrt{\epsilon_f^2 + 8\lambda^2}\Big) [|000\rangle + |110\rangle] \quad (47)$$
$$- \sqrt{8}\lambda [|101\rangle - |011\rangle] \Big\},$$

which is of the form in Eq. (12). We can therefore infer the concurrence from Eq. (13),

$$C(X_\infty) = \frac{1}{\sqrt{1 + X_\infty^2}}, \quad X_\infty = \sqrt{8}\lambda/\epsilon_f. \quad (48)$$

For $\epsilon_f \ll \lambda$, using Eq. (3), we thus obtain the conventional exponential decay of the concurrence with increasing distance between the MBSs, $C \sim \epsilon_f/\lambda \sim \exp(-L/\xi)$. For $\epsilon_f = 0$, the CAR contribution is precisely cancelled by the TP contribution corresponding to the second pair of states in Eq. (47), see also Eq. (13), and the concurrence vanishes identically.

On the other hand, for $\epsilon_f \gg \lambda$, we find $C = 1$ due to CAR processes, since entanglement is now dominated by the first pair of states in Eq. (47). The noninteracting system thus allows for CAR-mediated ideal entanglement as well, but $C = 1$ is reached only for rather small L where $\epsilon_f \gg \lambda$, see Eq. (3). For the realization of long-range entanglement, it is therefore essential to work with a floating island where $E_C \neq 0$.

We conclude that the noninteracting case can also be understood quantitatively in terms of a competition between TP and CAR processes. For even parity, we have seen that CAR processes dominate when a sizeable MBS hybridization ϵ_f is present, which effectively corresponds to a rather short distance L between the MBSs. We note that for odd parity, the role of TP and CAR processes is effectively interchanged, again yielding $C = 1$ for $\epsilon_f \gg \lambda$. Since we consider single-level dots and not metallic leads, otherwise competing processes such as normal reflection or local Andreev reflection [23, 30] are absent. As a consequence, the entanglement found in Eq. (48) is generally more robust.

C. MBS hybridization effects

For small L, the MBS hybridization ϵ_f may exceed the charging energy E_C significantly. We then consider the parameter regime (23) but with arbitrary ratio ϵ_f/E_C, i.e., both ϵ_f and E_C may be large compared to all other energy scales in the problem.

Gate parameter $n_g = 1$

Let us start with the case $n_g = 1$, assuming a symmetric setup, see Eq. (31). As shown before, for $\epsilon_f \ll E_C$, we then have $C = 1$ due to the TP mechanism. Now for finite (but large) $\epsilon_f < E_C$, the energy gap between the ground and excited state sectors in Eqs. (25) and (26) is given by $\Delta E = E_C - \epsilon_f$, see Fig. 2(a). However, as long as the condition in Eq. (23) continues to hold with the replacement $E_C \to \Delta E$, the situation remains conceptually as before, and for $\eta = 0$ (i.e., $n_g = 1$) and $E_C \to \Delta E$ in Eqs. (27)–(30), we again find $C = 1$.

On the other hand, for $\epsilon_f \gg E_C$, our $E_C = 0$ discussion suggests that the CAR mechanism generates full entanglement of the dots with $C = 1$ as well. We therefore now consider a finite (large) charging energy with $E_C < \epsilon_f$, where the previous ground and excited state sectors are effectively interchanged, $\mathcal{H}_0 \leftrightarrow \mathcal{H}_1$ in Eqs. (25) and (26). This situation is illustrated in Fig. 2(b), where we
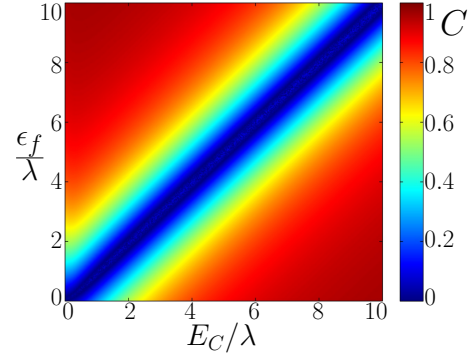

Figure 6. Color-scale plot of the concurrence for $n_g = 1$ in the ϵ_f-E_C plane, taking $E_J = \lambda$ and a symmetric system with $\epsilon = 0$, cf. Eq. (31).

can read off the energy gap separating the two sectors, $\Delta E' = \epsilon_f - E_C$. With the replacement $E_C \to \Delta E'$, we then assume that the condition in Eq. (23) holds again. In particular, the Josephson coupling E_J now directly connects the respective states in the low-energy sector such that the CAR processes needed for generating entanglement, cf. Sec. III B, are already captured by second-order perturbation theory, see Eq. (27). Considering the case $\epsilon_1 = -\epsilon_2$ and $\lambda_1 = \lambda_2 = \lambda$, and diagonalizing the remaining 4×4 Hamiltonian in the basis (26), we obtain the ground state

$$|\Psi\rangle = \mathcal{N}\Big\{(E_J/2)\left[|000,0\rangle + |110,1\rangle\right] \qquad (49)$$
$$+ \left(\Gamma + \sqrt{\Gamma^2 + (E_J/2)^2}\right)\left[|110,0\rangle + |000,1\rangle\right]\Big\},$$

where the rate

$$\Gamma = \lambda^2/\Delta E' = \lambda^2/(\epsilon_f - E_C) \qquad (50)$$

connects $|110,0\rangle$ and $|000,1\rangle$ through the virtual occupation of excited states. Although the concurrence formula (13) is not applicable for $|\Psi\rangle$ in Eq. (49), C can be computed analytically, with the result

$$C(X_f) = \frac{1}{\sqrt{1 + X_f^2}}, \quad X_f = 2\Gamma/E_J. \qquad (51)$$

In accordance with Sec. III B, the concurrence vanishes for $X_f \gg 1$, in particular for $E_J \to 0$.

These analytical results are nicely recovered from a numerically exact calculation of the concurrence for $n_g = 1$. We show a color-scale plot of C as a function of ϵ_f and E_C in Fig. 6, confirming that lines of constant concurrence are present when $\Delta E = -\Delta E' = E_C - \epsilon_f$ is held constant. We took $\epsilon_{1,2} = 0$ in Fig. 6, such that both TP and CAR processes can generate stable entanglement, see Sec. III. In the crossover regime $\epsilon_f \approx E_C$, we find a $C = 0$ line right at $\epsilon_f = E_C$, see Fig. 6. This limit is correctly captured from the CAR point of view (even though perturbation theory breaks down), since then the rate Γ in Eq. (50) becomes large and hence $C \to 0$ in Eq. (51).
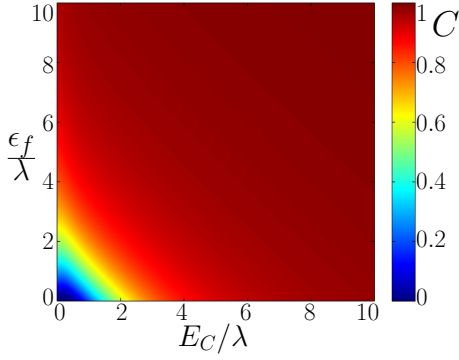
Figure 7. Same as Fig. 6 but for $n_g = 0$.

Approaching this limit from the TP-dominated side is more subtle. The energy diagrams in Fig. 2(a,b) reveal that there are six low-energy states at play for $\epsilon_f \approx E_C$. These states are directly coupled via $\lambda_{1,2}$ and E_J, which can be viewed as a mixing of TP and CAR processes. In that case, neither TP nor CAR are effective in generating entanglement anymore since the previously excited states may now be occupied as well.

Gate parameter $n_g = 0$

Finally, we turn to the case $n_g = 0$, where we consider optimal conditions for the CAR mechanism by choosing dot level energies with $\epsilon_1 = -\epsilon_2$ and symmetric tunnel couplings, $\lambda_1 = \lambda_2 = \lambda$. The corresponding energy diagram in Fig. 2(c) shows two out of the six possible CAR processes, see also Sec. III B. With the MBS hybridization ϵ_f, the first and the last state in Eq. (33) are still separated by the energy gap $4E_C$ from the ground state sector (32), while all other excited states in Eq. (33) have the gap $\Delta E_0 = E_C + \epsilon_f$. Depending on the ratio ϵ_f/E_C, different sequences out of the six possible CAR processes then become important. Nonetheless, as long as Eq. (23) holds for $E_C \to \min(4E_C, \Delta E_0)$, we may effectively apply Eq. (35) again. We thereby find $\tilde{H}$ as in Eq. (35) but with

$$b' \to b'' = -\left(\frac{1}{E_C + \epsilon_f} + \frac{1}{2E_C} \right) \frac{\lambda^2 E_J}{2(E_C + \epsilon_f)}, \quad (52)$$

where we set $\eta = 0$ (i.e., $n_g = 0$). The first term comes from the two CAR processes with excursions to $Q = \pm 1$ states, see Fig. 2(c), while the second term describes the remaining four CAR processes which also include a virtual occupation of $Q = \pm 2$ states. Regardless of which term dominates, throughout the regime $\Delta E_0 \gg \max(\lambda, E_J)$, we observe that CAR processes dominate the concurrence both for $E_C \gg \epsilon_f$ and for $\epsilon_f \gg E_C$. This fact can be rationalized by noting that the inversion of ground and excited state sectors (discussed for $n_g = 1$ above) does not take place anymore, since for arbitrary ratio ϵ_f/E_C, the states $|000,0\rangle$ and

$|110,0\rangle$ are lowest in energy. We therefore obtain $C = 1$ for almost the entire ϵ_f-E_C plane. The color-scale plot of the numerically exact solution in Fig. 7 confirms this result, with the region $\Delta E_0 \lesssim \lambda$ representing the only exception. In the latter region, one approaches the perfectly disentangled limit $\epsilon_f = E_C = 0$, where CAR and TP processes interfere destructively. Finally, we remark that lines of constant concurrence are visible in Fig. 7 when b'' in Eq. (52) is held fixed.

Concluding remarks

Although the above results follow with the replacements $E_C \to \Delta E, \Delta E', \Delta E_0$ in Eq. (23), we stress again that E_C itself has to remain large, $E_C > |\epsilon_{1,2}, \lambda_{1,2}, E_J|$. Otherwise the description via charging energy parabolas as in Fig. 2 is no longer sufficient and we expect deviations from the analytical results. Such deviations can be seen for $E_C \lesssim \lambda = E_J$ in Figs. 6 and 7, where one effectively approaches the noninteracting limit $E_C \to 0$.

V. ENTANGLEMENT DYNAMICS

Up to this point, we have studied the stationary case, with time-independent parameters in H. In this section, we address the entanglement dynamics, $C(t)$, observed after a quench of a tunnel coupling where, say, λ_2 is suddenly switched on from zero to a finite value at time $t = 0$. We assume that at times $t > 0$, we then have a symmetric system with $\epsilon = 0$ and $\lambda = 1$ in Eq. (31), and we again consider the even-parity sector, $\mathcal{P} = +1$.

Studies of the entanglement dynamics can be very useful in revealing important timescales of the problem [44, 49]. We will see below that similar to the static case in Sec. IV, perturbation theory is helpful in elucidating the underlying physical mechanisms and the relevant timescales governing $C(t)$. In particular, our results for $C(t)$ can again be interpreted in terms of TP and CAR processes.

A. Finite charging energy: $n_g = 1$

Let us begin with the case of finite E_C and arbitrary ϵ_f, keeping $\Delta E = E_C - \epsilon_f > 0$, see Sec. IV C. For simplicity, we put $E_J = 0$ and $n_g = 1$, where we expect that entanglement is mediated by TP processes. We note in passing that in the presence of weak parity-breaking processes, e.g., due to quasiparticle poisoning, the even total parity ($\mathcal{P} = +1$) sector is the true ground state at $n_g = 1$. Suddenly switching on the tunnel coupling $\lambda_2 = 0 \to \lambda$ at time $t = 0$ results in a time-dependence of the concurrence, where our numerical results for $C(t)$ are shown in Fig. 8. Here we start out from the initial state $|\Psi(t < 0)\rangle = |101,0\rangle$, where the decoupled dot (QD$_2$
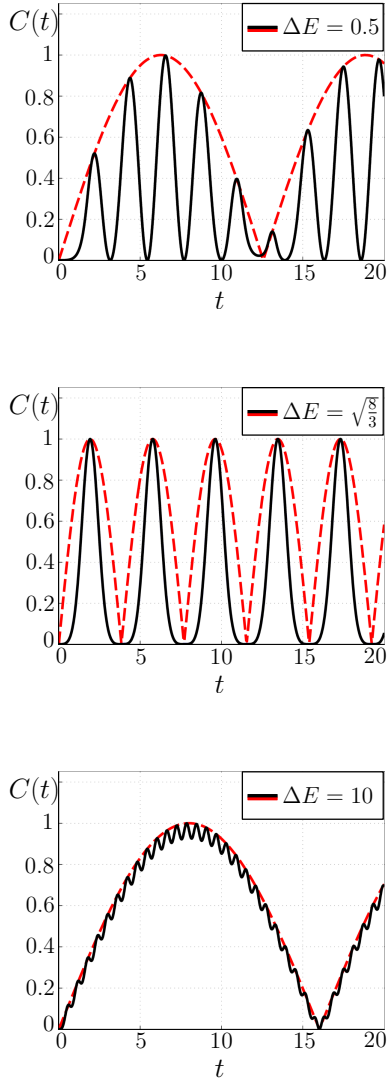
Figure 8. Time-dependence of the concurrence, $C(t)$, obtained after a quench of the tunnel coupling, $\lambda_2 = 0 \to 1$ at $t = 0$, for three different values of $\Delta E = E_C - \epsilon_f$. We consider the case of finite E_C with $n_g = 1$, taking $E_J = \epsilon_{1,2} = 0$ and $\lambda_1 = 1$. Exact results (black solid curves) follow from Eqs. (53) and (54). The envelope functions (red dashed curves) in Eq. (55) accurately capture the slow part of the dynamics.

in Fig. 1) is empty before the quench. The post-quench state $|\Psi(t > 0)\rangle$ is of the form

$$|\Psi(t)\rangle = c_1(t)|110,0\rangle + c_2(t)|101,0\rangle \quad (53)$$
$$+ c_3(t)|011,0\rangle + c_4(t)|000,1\rangle,$$

where the time-dependent coefficients $c_j(t)$ are subject to normalization, $\sum_j c_j(t) = 1$, and obey the initial con-

dition $c_j(0) = \delta_{j,2}$. The solution is given by

$$c_1(t) = -c_4(t) = \frac{-i\lambda}{\sqrt{2}\Omega} e^{-iE_C t/2} \sin(\Omega t), \quad (54)$$

$$c_2(t) = \frac{e^{-i\epsilon_f t/2}}{2} + \frac{e^{-iE_C t/2}}{2\Omega} \left[\frac{i\Delta E}{2} \sin(\Omega t) + \Omega \cos(\Omega t) \right],$$

$$c_3(t) = e^{-i\epsilon_f t/2} - c_2(t),$$

where $\Omega = \sqrt{(\Delta E/2)^2 + 2\lambda^2}$. The concurrence $C(t)$ then follows by inserting the coefficients in Eq. (54) into Eq. (13). Since for $E_J = 0$, total particle number is conserved, only the given four states in Eq. (53) with same total particle number as in the initial state are accessible. For that reason, Eqs. (53) and (54) represent the exact solution for arbitrary $\Delta E > 0$ as long as $E_J = 0$. Indeed, the $C(t)$ results in Fig. 8 are identical to those obtained from numerically solving the full Schrödinger equation.

To gain physical intuition, it is instructive to compare these exact (but not very illuminating) results for $C(t)$ to the corresponding predictions obtained from the reduced 2×2 Hamiltonian $\tilde{H}$ in Eq. (28), with the replacement $E_C \to \Delta E$ as in Sec. IV C. Using the parameters a and b in $\tilde{H}$, only a single oscillation frequency, $\omega_p = 2\sqrt{a^2 + b^2}$, appears within that approach, where for our symmetric system, we find $\omega_p = 2\lambda^2/\Delta E$. The low-energy Hamiltonian $\tilde{H}$ captures only the slow part of the dynamics, i.e., the envelope function $C_e(t)$. Moreover, its perturbative derivation requires the condition $\Delta E \gg \lambda$. On the other hand, for $\Delta E \lesssim \lambda$, we can directly separate the slow and fast variations in the full analytical expression for $C(t)$ described above, which gives $C_e(t)$ also for $\Delta E \lesssim \lambda$. Combining both cases, we obtain a sinusoidal envelope function,

$$C_e(t) = |\sin(\omega_e t)|, \quad (55)$$

with the frequency

$$\omega_e = \begin{cases} \Delta E/2, & \Delta E/\lambda < \sqrt{8/3}, \\ \sqrt{(\Delta E/2)^2 + 2\lambda^2} - \Delta E/2, & \Delta E/\lambda > \sqrt{8/3}. \end{cases} \quad (56)$$

Notice that for $\Delta E/\lambda < \sqrt{8/3}$, the slow part of the dynamics becomes universal (independent of the tunnel coupling λ). For $\Delta E/\lambda \approx \sqrt{8/3}$, $C(t)$ is governed by two almost resonant frequencies and the envelope function in Eq. (55) becomes less meaningful. Figure 8 illustrates that away from this (quite narrow) transition regime, Eqs. (55) and (56) accurately describe the slow envelopes of all $C(t)$ curves. For $\Delta E \gg \lambda$, the frequency ω_e in Eq. (56) coincides with the perturbative scale ω_p extracted from $\tilde{H}$. In this limit, Eq. (55) becomes exact, $C(t) \to C_e(t)$, and the fast oscillations in $C(t)$ disappear altogether, cf. Fig. 8. By comparing the characteristic frequencies appearing in the exact solution for $C(t)$ to perturbative estimates valid for $\Delta E \gg \lambda$, we thus have complemented our picture of the system in Fig. 2.

B. Finite charging energy: $n_g = 0$

Such an analysis of the entanglement dynamics becomes more difficult for other parameters within the large-E_C regime, We here briefly consider the case $n_g = 0$ with $E_J > 0$, where CAR processes can establish entanglement. The Josephson coupling now makes the inclusion of higher-energy states with different total particle numbers necessary, and exact expressions for the envelope curves as in Eqs. (55) and (56) are more challenging to obtain. Nonetheless, analytical estimates are still possible in the perturbative regime, where we obtain $C_e(t)$ as in Eq. (55) but with $\omega_e \approx \omega_p = 2|b''|$, using b'' in Eq. (52). The CAR-induced entanglement dynamics at $n_g = 0$ is thus characterized by a sinusoidal envelope function again but has the rather long timescale $\sim E_C^2/(\lambda^2 E_J)$.

C. Noninteracting case

Another case of interest that allows for an exact solution is given by $E_C = 0$. Since the Cooper pair sector decouples, see Sec. IV B, we then have a set of four states describing the full dynamics again. The concurrence dynamics after a tunnel coupling quench was recently addressed for this limit of our setup in Ref. [25], where oscillations in $C(t)$ were reported as well. With $\epsilon_f > 0$, taking the pre-quench ground state $|\Psi(t < 0)\rangle = |110\rangle$, and expanding $|\Psi(t)\rangle$ in terms of the four basis states available for even parity and $E_C = 0$, the post-quench ($t > 0$) state is as in Eq. (53) but with the initial condition $c_j(0) = \delta_{j,1}$. By solving the time-dependent Schrödinger equation as detailed in Ref. [25], $C(t)$ follows again from Eq. (13).

In fact, even though CAR processes are now responsible for generating entanglement, finding $C(t)$ for $E_C = 0$ is fully equivalent to the TP-mediated case in Sec. V A after replacing $\Delta E = E_C - \epsilon_f \to \epsilon_f$. We thus obtain the same concurrence dynamics as in Eqs. (55) and (56) after this replacement [50], including the results shown in Fig. 8, where now $\epsilon_f \approx \lambda$ separates the perturbative regime ($\epsilon_f \gg \lambda$) from the regime where calculation of $C(t)$ needs to account for all four states ($\epsilon_f \lesssim \lambda$), see Eqs. (47) and (48).

VI. CONCLUSIONS

In this paper, we have provided a detailed study of entanglement in a floating topological superconducting island hosting a pair of MBSs, each of which is tunnel-coupled to a single-level dot. The concurrence then provides a convenient measure to quantify entanglement of the two dots. We have shown that this setup offers a robust route towards the implementation of a "Majorana entanglement bridge" where the concurrence does not exhibit any decay with increasing separation of the MBSs. The only restriction for the separation of the quantum dots then is given by requiring a finite charging energy

on the island, yielding much longer ranges of entanglement than in usual notions of exponential decay. This unique behavior is due to the intrinsic nonlocality of the fermion state representing the pair of MBSs. The underlying mechanisms for entanglement generation have been identified in an intuitive yet quantitative manner. In particular, we have shown that entanglement is created by the interplay of teleportation and crossed Andreev reflection processes. With this understanding, we were then able to discuss the more complicated entanglement dynamics after the quench of a tunnel coupling in terms of simple envelope functions.

We have studied entanglement for the Majorana device in Fig. 1 by employing the concurrence as entanglement measure. Although the concurrence has a rather formal definition, the predicted entanglement features should be observable in mesoscopic transport experiments, where the two dots are weakly coupled to additional leads as described, e.g., in Ref. [51]. Since current-current correlation functions can detect the violation of Bell inequalities [52], signatures of entanglement are expected to appear in shot noise measurements, see also Refs. [53–55] for related proposals. In principle also suitably designed conductance measurements could probe entanglement [56].

Recent experimental work [4, 5, 45, 46] indicates that devices corresponding to the model studied here are in close reach. For instance, charging energies of order $E_C \approx 1$ meV and TS gaps $\Delta \approx 0.2$ meV have been reported in Ref. [46], where quantum dots can be formed spontaneously near the TS wire ends when contacting them by Au leads [57]. In order to reach the regime $\Delta > E_C$ assumed in our model, the charging energy could be lowered by simply increasing the wire length. On the other hand, it may be possible to achieve significant entanglement between the dots even when $\Delta < E_C$, where fermionic TS quasiparticles should be taken into account. When such states are localized in the bulk of the TS such that they do not have significant overlap with the Majorana bound states, they have no effect on entanglement. When low-lying quasiparticle states are localized near the TS nanowire ends, the physics discussed here may change, but entanglement may nonetheless be possible according to our preliminary analysis, see also Ref. [29]. Using NbTiN [45] or InAs/Al [46] to proximity-induce superconductivity in a device similar to the one in Fig. 1, extremely small poisoning rates have been reported as well. In any case, a detailed study of quasiparticle effects on entanglement is beyond the scope of the present work.

To conclude, we are confident that future theoretical and experimental studies of similar setups utilizing such a Majorana entanglement bridge will benefit from the detailed physical understanding supplied here.

[1] J. Alicea, *New directions in the pursuit of Majorana fermions in solid state systems*, Rep. Prog. Phys. **75**, 076501 (2012).

[2] M. Leijnse and K. Flensberg, *Introduction to topological superconductivity and Majorana fermions*, Semicond. Sci. Techn. **27**, 124003 (2012).

[3] C.W.J. Beenakker, *Search for Majorana Fermions in Superconductors*, Annu. Rev. Condens. Matter Phys. **4**, 113 (2013).

[4] V. Mourik, K. Zuo, S.M. Frolov, S.R. Plissard, E.P.A.M. Bakkers, and L.P. Kouwenhoven, *Signatures of Majorana fermions in hybrid superconductor-semiconductor nanowire devices*, Science **336**, 1003 (2012).

[5] L. Rokhinson, X. Liu, and J. Furdyna, *The fractional a.c. Josephson effect in a semiconductor-superconductor nanowire as a signature of Majorana particles*, Nature Physics **8**, 795 (2012).

[6] A. Das, Y. Ronen, Y. Most, Y. Oreg, M. Heiblum, and H. Shtrikman, *Zero-bias peaks and splitting in an Al-InAs nanowire topological superconductor as a signature of Majorana fermions*, Nat. Phys. **8**, 887 (2012).

[7] M.T. Deng, C.L. Yu, G.Y. Huang, M. Larsson, P. Caroff, and H.Q. Xu, *Anomalous Zero-Bias Conductance Peak in a Nb-InSb Nanowire-Nb Hybrid Device*, Nano Lett. **12**, 6414 (2012).

[8] H.O.H. Churchill, V. Fatemi, K. Grove-Rasmussen, M.T. Deng, P. Caroff, H.Q. Xu, and C.M. Marcus, *Superconductor-nanowire devices from tunneling to the multichannel regime: Zero-bias oscillations and magnetoconductance crossover*, Phys. Rev. B **87**, 241401(R) (2013).

[9] E.J.H. Lee, X.C. Jiang, M. Houzet, R. Aguado, C.M. Lieber, and S. De Franceschi, *Spin-resolved Andreev levels and parity crossings in hybrid superconductor-semiconductor nanostructures*, Nature Nanotech. **267**, 79 (2014).

[10] S. Nadj-Perge, I.K. Drozdov, J. Li, H. Chen, S. Jeon, J. Seo, A.H. MacDonald, B. Andrei Bernevig, and A. Yazdani, *Observation of Majorana fermions in ferromagnetic atomic chains on a superconductor*, Science **346**, 602 (2014).

[11] F. Hassler, A.R. Akhmerov, C.Y. Hou, and C.W.J. Beenakker, *Anyonic interferometry without anyons: how a flux qubit can read out a topological qubit*, New J. Phys. **12**, 125002 (2010).

[12] J.D. Sau, S. Tewari, and S. Das Sarma, *Universal quantum computation in a semiconductor quantum wire network*, Phys. Rev. A **82**, 052322 (2010).

[13] K. Flensberg, *Non-Abelian Operations on Majorana Fermions via Single-Charge Control*, Phys. Rev. Lett. **106**, 090503 (2011).

[14] L. Jiang, C.L. Kane, and J. Preskill, *Interface between Topological and Superconducting Qubits*, Phys. Rev. Lett. **106**, 130504 (2011).

[15] P. Bonderson and R.M. Lutchyn, *Topological Quantum Buses: Coherent Quantum Information Transfer between Topological and Conventional Qubits*, Phys. Rev. Lett. **106**, 130505 (2011).

[16] M. Leijnse and K. Flensberg, *Quantum Information Transfer between Topological and Spin Qubit Systems*, Phys. Rev. Lett. **107**, 210502 (2011).

[17] M. Leijnse and K. Flensberg, *Hybrid topological-spin qubit systems for two-qubit-spin gates*, Phys. Rev. B **86**, 104511 (2012).

[18] T. Hyart, B. van Heck, I.C. Fulga, M. Burrello, A.R. Akhmerov, and C.W.J. Beenakker, *Flux-controlled quantum computation with Majorana fermions*, Phys. Rev. B **88**, 035121 (2013).

[19] Yu.V. Nazarov and Ya.M. Blanter, *Quantum transport: Introduction to Nanoscience* (Cambridge University Press, Cambridge, UK, 2009).

[20] R. Horodecki, P. Horodecki, M. Horodecki, and K. Horodecki, *Quantum entanglement*, Rev. Mod. Phys. **81**, 865 (2009).

[21] G. Semenoff and P. Sodano, *Stretching the electron as far as it will go*, Electron. J. Theor. Phys. **10**, 157 (2006).

[22] C.J. Bolech and E. Demler, *Observing Majorana bound states in p-wave superconductors using noise measurements in tunneling experiments*, Phys. Rev. Lett. **98**, 237002 (2007).

[23] J. Nilsson, A.R. Akhmerov, and C.W.J. Beenakker, *Splitting of a Cooper Pair by a Pair of Majorana Bound States*, Phys. Rev. Lett. **101**, 120403 (2008).

[24] S. Tewari, C. Zhang, S. Das Sarma, C. Nayak, and D.H. Lee, *Testable Signatures of Quantum Nonlocality in a Two-Dimensional Chiral p-Wave Superconductor*, Phys. Rev. Lett. **100**, 027001 (2008).

[25] J. Li, T. Yu, H.Q. Lin, and J.Q. You, *Probing the nonlocality of Majorana fermions via quantum correlations*, Sci. Rep. **4**, 4930 (2014).

[26] A. Zazunov, P. Sodano, and R. Egger, *Even-odd parity effects in Majorana junctions*, New J. Phys. **15**, 035033 (2013).

[27] S. Bose, *Quantum communication through an unmodulated spin chain*, Phys. Rev. Lett. **91**, 207901 (2003).

[28] A. Bayat, S. Bose, and P. Sodano, *Entanglement routers using macroscopic singlets*, Phys. Rev. Lett. **105**, 187204 (2010).

[29] M. Leijnse and K. Flensberg, *Coupling Spin Qubits via Superconductors*, Phys. Rev. Lett. **111**, 060501 (2013).

[30] L. Fu, *Electron Teleportation via Majorana Bound States in a Mesoscopic Superconductor*, Phys. Rev. Lett. **104**, 056402 (2010).

[31] A. Zazunov, A.L. Yeyati, and R. Egger, *Coulomb blockade of Majorana-fermion-induced transport*, Phys. Rev. B **84**, 165440 (2011).

[32] R. Hützen, A. Zazunov, B. Braunecker, A.L. Yeyati, and R. Egger, *Majorana Single-Charge Transistor*, Phys. Rev.

Lett. **109**, 166403 (2012).

[33] Z. Wang, X.Y. Hu, Q.F. Liang, and X. Hu, *Detecting Majorana fermions by nonlocal entanglement between quantum dots*, Phys. Rev. B **87**, 214513 (2013).

[34] S. Walter and J.C. Budich, *Teleportation-induced entanglement of two nanomechanical oscillators coupled to a topological superconductor*, Phys. Rev. B **89**, 155431 (2014).

[35] In particular, the authors of Ref. [33] studied the large-E_C limit with $\epsilon_f = 0$ in a Coulomb valley (integer n_g) by fixing the number of Cooper pairs, and reported long-range entanglement in this limit. By means of a master equation approach, Ref. [34] arrived at similar conclusions when the dots are replaced by nanomechanical oscillators.

[36] B. Béri and N.R. Cooper, *Topological Kondo Effect with Majorana Fermions*, Phys. Rev. Lett. **109**, 156803 (2012).

[37] A. Altland and R. Egger, *Multiterminal Coulomb-Majorana Junction*, Phys. Rev. Lett. **110**, 196401 (2013).

[38] B. Béri, *Majorana-Klein Hybridization in Topological Superconductor Junctions*, Phys. Rev. Lett. **110**, 216803 (2013).

[39] A. Altland, B. Béri, R. Egger, and A.M. Tsvelik, *Multichannel Kondo Impurity Dynamics in a Majorana Device*, Phys. Rev. Lett. **113**, 076401 (2014).

[40] A. Zazunov, A. Altland, and R. Egger, *Transport properties of the Coulomb-Majorana junction*, New J. Phys. **16**, 015010 (2014).

[41] D.E. Drummond, A.A. Kovalev, C.Y. Hou, K. Shtengel, and L.P. Pryadko, *Demonstrating entanglement by testing Bell's theorem in Majorana wires*, Phys. Rev. B **90**, 115404 (2014).

[42] G.B. Lesovik, T. Martin, and G. Blatter, *Electronic entanglement in the vicinity of a superconductor*, Eur. Phys. J. B **24**, 287 (2001).

[43] P. Recher, E.V. Sukhorukov, and D. Loss, *Andreev tunneling, Coulomb blockade, and resonant transport of nonlocal spin-entangled electrons,* Phys. Rev. B **63**, 165314 (2001).

[44] P. Sodano, A. Bayat, and S. Bose, *Kondo cloud mediated long-range entanglement after local quench in a spin chain*, Phys. Rev. B **81**, 100412(R) (2010).

[45] D.J. van Woerkom, A. Geresdi, and L.P. Kouwenhoven, *1 minute parity lifetime of a NbTiN Cooper-pair transistor,* preprint arXiv:1501.03855.

[46] A.P. Higginbotham, S.M. Albrecht, G. Kirsanskas, W. Chang, F. Kuemmeth, P. Krogstrup, T.S. Jespersen, J. Nygård, K. Flensberg, and C.M. Marcus, *Parity lifetime of bound states in a proximitized semiconductor nanowire,* preprint arXiv:1501.05155.

[47] S. Bravyi, D.P. DiVincenzo, and D. Loss, *Schrieffer-Wolff transformation for quantum many-body systems,* Ann. Phys. **326**, 2793 (2011).

[48] The general expression for $H^{(3)}$ [47] is of symmetrized form with respect to the initial and final state energies E_{ν_0} and $E_{\nu_0'}$, cf. also Eq. (27). Since those two energies here coincide, we obtain the simpler result in Eq. (34).

[49] P.A. Oliveira and L. Sanz, *Bell states and entanglement dynamics on two coupled quantum molecules*, Ann. Phys. (in press), see arXiv:1503.00928.

[50] At first sight, it might be confusing that even though entanglement was generated by TP in Sec. V A, CAR processes here yield practically the same results (with the above replacements). However, note that for $E_C = 0$, the Cooper pair sector decouples completely. Therefore, TP and CAR effectively become equivalent virtual transition processes that only act on different sets of states, see Secs. IV B and IV C.

[51] S. Gustavsson, R. Leturcq, M. Studer, I. Shorubalko, T. Ihn, K. Ensslin, D.S. Driscoll, and A.C. Gossard, *Electron Counting in quantum dots*, Surf. Sci. Rep. **64**, 191 (2009).

[52] N.M. Chtchelkatchev, G. Blatter, G.B. Lesovik, and T. Martin, *Bell inequalities and entanglement in solid-state devices*, Phys. Rev. B **66**, 161320(R) (2002).

[53] D. Loss and E.V. Sukhorukov, *Probing entanglement and nonlocality of electrons in a double-dot via transport and noise*, Phys. Rev. Lett. **84**, 1035 (2000).

[54] P. Samuelsson, E.V. Sukhorukov, and M. Büttiker, *Orbital Entanglement and Violation of Bell Inequalities in Mesoscopic Conductors*, Phys. Rev. Lett. **91**, 157002 (2003).

[55] M. Blaauboer and D.P. DiVincenzo, *Detecting Entanglement Using a Double-Quantum-Dot Turnstile*, Phys. Rev. Lett. **95**, 160402 (2005).

[56] B. Braunecker, P. Burset, and A. Levy Yeyati, *Entanglement Detection from Conductance Measurements in Carbon Nanotube Cooper Pair Splitters*, Phys. Rev. Lett. **111**, 136806 (2013).

[57] S.M. Albrecht and C.M. Marcus, private communication.